Highly Compressible 3D-Printed Soft Magnetoelastic Sensors for Human−Machine Interfaces

Hyeonseo Song,[#] Yeonwoo Jang,[#] Jin Pyo Lee, Jun Kyu Choe, Minbyeol Yun, Youn-Kyoung Baek, and Jiyun Kim[*]

Cite This: ACS Appl. Mater. Interfaces 2023, 15, 59776−59786

Read Online

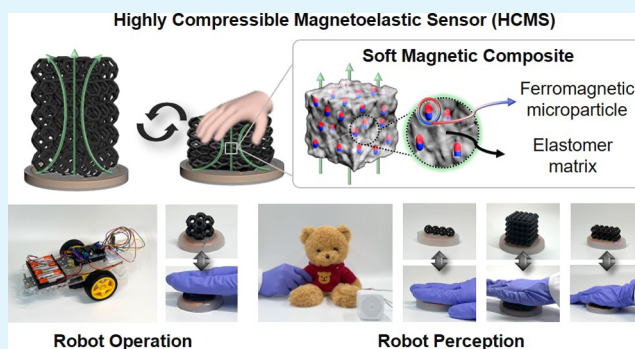ACCESS | Metrics & More | Article Recommendations | Supporting Information

ABSTRACT: Incorporating perception into robots or objects holds great potential to revolutionize daily human life. To achieve this, critical factors include the design of an integrable three-dimensional (3D) soft sensor with self-powering capability, a wide working range, and tuneable functionalities. Here, we introduce a highly compressible 3D-printed soft magnetoelastic sensor with a wide strain sensing range. Inspired by the lattice metamaterial, which offers a highly porous structure with tuneable mechanical properties, we realized a remarkably compliant 3D self-powering sensor. Using magnetoelastic composite materials and 3D printing combined with sacrificial molding, a broad design space for constituent materials and structures is investigated, allowing for tuneable mechanical properties and sensor performances. These sensors are successfully integrated with two robotic systems as the robot operation and perception units, enabling robot control and recognition of diverse physical interactions with a user. Overall, we believe that this work represents a cornerstone for compliant 3D self-powered soft sensors, giving impetus to the development of advanced human−machine interfaces.

KEYWORDS: magnetoelastic effect, soft magnetic composite, 3D printing, lattice structure, soft sensor, human−machine interface

Highly Compressible Magnetoelastic Sensor (HCMS)
Soft Magnetic Composite
Ferromagnetic microparticle
Elastomer matrix
Robot Operation
Robot Perception

1. INTRODUCTION

Tactile sensors for human−machine interfaces (HMIs) have gained significant attention in healthcare systems, virtual reality, and robotics.[1−6] They convert mechanical stimuli into electrical signals, providing immersive user experiences and optimized responses while interacting with machines. Soft tactile sensors have great potential for safe and adaptable human and environmental interactions compared to conventional sensors made of rigid materials.[7−9] Nevertheless, conventional passive soft sensors usually rely on extra power sources and components such as commercial batteries.[10,11] These dependencies restrict sensor flexibility and increase production and maintenance costs.

Recent approaches have exploited sensing mechanisms such as triboelectric,[12−16] piezoelectric,[5,17−20] magnetoelastic,[21−23] and magnetoelectric[24−26] methods to develop fully soft, self-powered sensors that do not need external power sources for signal production. However, triboelectric and piezoelectric sensors exhibit high internal impedance, which lowers the current flow, diminishing the current and output power densities. Furthermore, high humidity in the environment, including sweat on the skin, can impact the output sensing performance of triboelectric and piezoelectric sensors due to changes in the surrounding environment's dielectric constant, affecting the electric charge transfer and capacitance.

Conversely, magnetoelastic sensors, which implement Faraday's law, have been shown to exhibit a low internal impedance, a high current density, and even waterproof capabilities. Thus, a soft self-powered tactile sensor utilizing a magnetoelastic mechanism can potentially offer high output power densities and a more reliable output performance, enabling it to function as a perception unit in numerous distinctive and practical interaction scenarios in HMI applications.

In previous studies, soft magnetoelastic sensors were mostly fabricated with a membrane-based two-dimensional (2D) form factor, using a composite of magnetic particles with liquid metals or conductive yarns.[21−23] This 2D form factor offers advantages for wearable electronics due to its capability of conformally attaching to body surfaces. However, it still has limitations in designing 3D architectures with appropriate structural and mechanical properties for a seamless fit with daily life objects. To overcome these limitations, previous
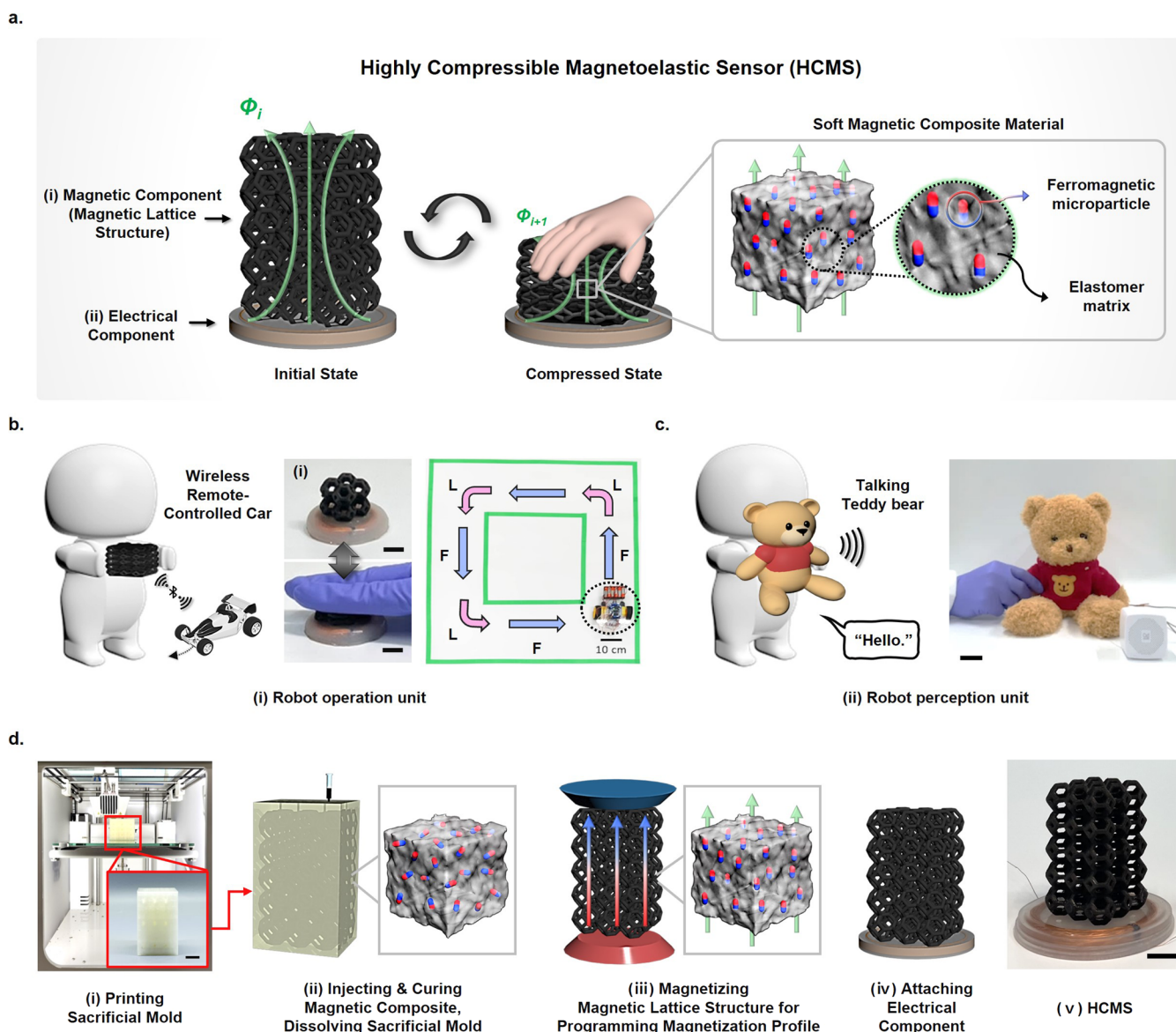
Figure 1. Overall schematic including sensing mechanism, applications, and fabrication of the HCMSs. (a) Conceptual schematic for sensing mechanism of the self-powered HCMSs composed of the magnetic and electrical components. (b,c) Schematic for two different robotic applications of the HCMSs. Scale bars are 10 mm. (d) Fabrication process of the HCMSs. Scale bar is 10 mm.

studies demonstrated a sensor with a helical coil and magnetic composite produced with a simple 3D-printed mold employing a simple topology.[24−26] Nevertheless, the mechanical properties of the solid cubic-like polymeric structure resulted in the sensor presenting limited compressibility, reaching only up to 20% strain.[24] To improve the compressibility, a different study printed a sensor with a porous magnetic structure containing a conductive helix coil. However, the sensor still exhibited low compressibility (20% strain) due to its relatively brittle material properties.[25] Recently, a more compressible 3D magnetoelastic sensor with a stepwise structure has been reported. In this sensor, the compressible porous part, responsible for generating significant strain under compression, was entirely 3D-printed using thermoplastic polyurethane (TPU) material. However, the functional magnetic component located on top of the porous TPU structure maintained a solid cubic-like structure. The presence of this unnecessary non-magnetic and nonelectrical component, which is essential to

achieve significant compressibility, limits the design capability of the 3D sensor.[26]

Here, we introduce a highly compressible magnetoelastic sensor (HCMS) with a detectable strain range of up to 91% and programmable mechanical properties. To achieve this, we developed a flexible lattice mechanical metamaterial with magnetic composites to create a highly porous and mechanically tuneable 3D structure by using the sacrificial mold 3D printing method. Our printing method allows us to design any scale, shape, and topology of the lattice metamaterial. Moreover, numerous polymeric matrices and magnetic materials can be chosen and injected into the printed mold. As the lattice structure containing magnetic composites is deformed, the magnetic flux density passing through the cross-sectional area of the coil wire at the bottom changes, thus, inducing an electrical signal. Hence, using our 3D printing method, we demonstrate that the detectable strain range and electrical performance of HCMS can be tailored by adjusting the material, structural, and systematic parameters,
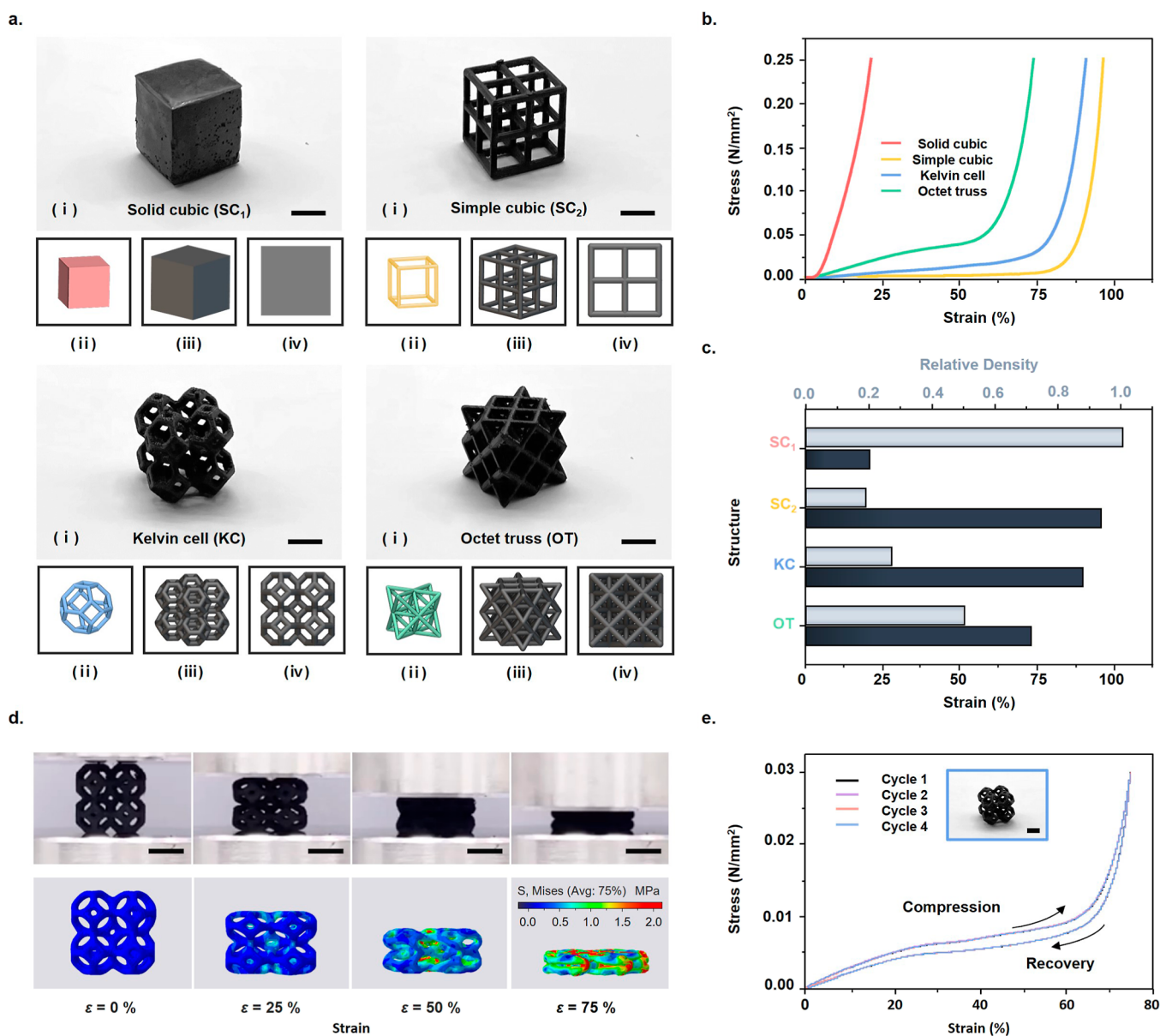
Figure 2. Programmable mechanical properties of the magnetic components of the HCMSs. (a) Solid cubic magnetic structures and representative magnetic lattice structures such as simple cubic, Kelvin cell, and octet truss. (i) Real images, (ii) schematic images of the $1 \times 1 \times 1$ unit structure, (iii) schematic images of the entire $2 \times 2 \times 2$ lattice structure in the perspective view, and (iv) schematic images of the entire $2 \times 2 \times 2$ structure in the top view. Scale bars are 10 mm. (b) Stress−strain curve for the solid cubic, simple cubic, Kelvin cell, and octet truss structures. (c) Compression strain and relative density for the solid cubic, simple cubic, Kelvin cell, and octet truss structures. (d) Experimental results and finite-element simulations for a compression test for a magnetic Kelvin cell structure with $2 \times 2 \times 2$ K unit cells. Scale bars are 10 mm. (e) Cyclic compression test of the magnetic Kelvin cell structure in four continuously repeated cycles.

including magnetic microparticle concentration, lattice structure, sensor shape and scale, and coil geometries.

To demonstrate the practical potential of HCMSs, we used them as robot control and perception units. First, we used the HCMS as a controller for a wireless remote-controlled (RC) car. According to users' gestures and a robotic control strategy, electrical signals from our HCMS provide directional feedback to the RC car, facilitating control of the movement direction. In addition, we embedded various shapes of HCMSs into a plush toy to create a talking teddy bear (MILAB toy) that can sense the users' physical interaction and respond with speech. We anticipate that HCMSs provide a novel design method for self-powered soft sensors and encourage the improvement of the HMI for everyday applications.

2. RESULTS AND DISCUSSION

2.1. Principle and Fabrication of HCMS. We present a simple process using a commercial 3D printer to design and fabricate a highly compressible 3D-printed HCMS capable of self-powered sensing. As shown in Figures 1a, S1, and 2, HCMSs consist of an electrical component, which has a metal coil embedded in a flexible elastomeric matrix to receive the electromotive force (EMF) generated by the magnetic flux change, and a magnetic component, which is a 3D lattice structure composed of a magnetic composite material to generate a magnetic flux change by structural deformation. The overall concentration of magnetic microparticles and the magnetization profile of the entire structure vary depending
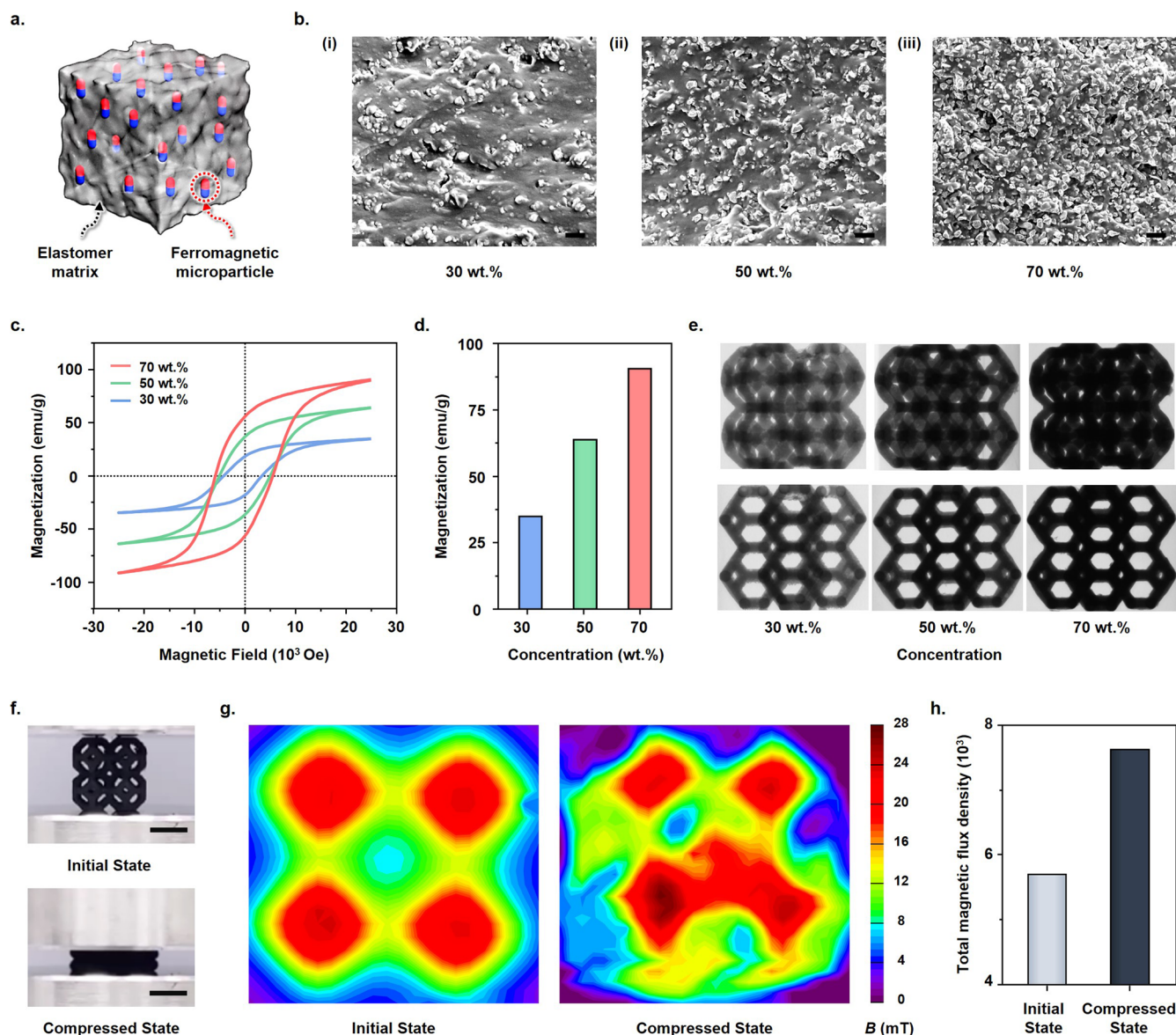
Figure 3. Programmable magnetic properties of the magnetic component of the HCMS. (a,b) Schematic and SEM images of the magnetic composite with different concentrations which were injected into the internal channel of the sacrificial mold to fabricate the HCMS. (i) 30, (ii) 50, and (iii) 70 wt %. Scale bars are 20 μm. (c−e) Magnetic hysteresis loop, saturation magnetization, micro-CT images of magnetic composite with 30, 50, and 70 wt % magnetic particle concentration. (f) Side view images of 2 × 2 × 2 K cell structures with 70 wt % magnetic particle concentration in initial and compressed states (75% strain). Scale bars are 10 mm. (g) Magnetic flux density mapping of 2 × 2 × 2 K cell structures with 70 wt % magnetic particle concentration in the initial and compressed state. (h) Total magnetic flux density of 2 × 2 × 2 K cell structures with 70 wt % magnetic particle concentration in the initial and compressed state.

on whether it is in the initial or compressed state. In the initial state, the HCMS is designed with a uniformly programmed magnetization profile along its z-axis by magnetizing the entire structure during fabrication. When the HCMS is subjected to mechanical stimuli, the resulting shape deformation alters the concentration of magnetic microparticles within the magnetic component and the overall magnetization profile of the magnetic component, inducing a magnetic flux change of the entire structure. According to Faraday's law of induction, magnetic flux changes through a circuit loop result in a voltage.[27]

Thus, by detection of the induced electrical voltage output, external mechanical stimuli applied to the HCMS can be detected. The induced electrical voltage can be calculated by eq 1 as follows

$$E(V) = -N\frac{\Delta\varnothing}{\Delta t} = -\sum_{i=1}^{i}\frac{\Delta\varnothing_i}{\Delta t} = -\sum_{i=1}^{i}\frac{\varnothing_{i+1} - \varnothing_i}{\Delta t} \quad (1)$$

where $E(V)$ is the output voltage, N is the number of turns, $\Delta\varphi$ is the total magnetic flux change, and Δt is the compression time of the soft HCMS. Additionally, we demonstrated the large potential of HCMSs for HMI applications by using our HCMSs as real-time robot operation/perception units (Figure 1b,c).

The fabrication process for HCMS composed of magnetic and electrical components is illustrated in Figure 1d. First, we printed a 3D sacrificial mold with an internal channel network for magnetic composite injection using poly(vinyl alcohol) (PVA) filaments. Second, neodymium−iron−boron (NdFeB) microparticles were prepared and mixed with a viscous

elastomer in the liquid state to form a homogeneous magnetic composite. Third, the magnetic composite was injected into the internal channel network of the 3D-printed sacrificial mold. Then, we polymerized the magnetic composite by applying external heat and immersed the resulting PVA mold in a water bath to dissolve it. After the dissolving process, a magnetic lattice structure that was uniformly magnetized along its z-axis was achieved. Finally, the magnetic lattice structure was integrated with coiled copper wires embedded in an Ecoflex to construct the HCMS. This fabrication process allows us to fabricate magnetic components of any topology, shape, and scale with any material that can be injected and thermally polymerized within the internal channel network of the sacrificial mold. Consequently, this method expands the design space of HCMS beyond conventional soft sensors. It allows for choosing the magnetic properties of the soft material, the mechanical properties of the sensor body, the overall shape of the sensor, and other factors that directly impact the output performance. To expand the design space and systemize the design parameters of HCMSs, we designed the magnetic component by adjusting the lattice parameters.

2.2. Mechanical Characteristics of the Magnetic Component of HCMS.

As shown in Figure 2a, we used a solid cubic structure and other representative lattice structures such as simple cubic, Kelvin cells, and octet truss, containing 70 wt % NdFeB magnetic microparticles embedded in an elastomer matrix with a size of $20 \times 20 \times 20$ mm^3. The stress–strain curves in Figure 2b show the mechanical behavior after a compression test. Compared with the other lattice structures, the solid cubic structure exhibits maximum stiffness, implying that its lattice structure provides mechanical advantages for the design of a highly compressible structure. Moreover, even though the octet truss structure is a representative stretching-dominated structure, it shows lower elasticity compared to the simple cubic and Kelvin cell structures, which are considered bending-dominated structures (Table S1 and Figure S3).[28−31] Specifically, the solid cubic, simple cubic, Kelvin cell, and octet truss structures show compression strains (ε) of 21, 97, 91, and 74%, respectively. The selection of a specific lattice structure can be chosen to match common interaction pattern characteristics of the intended applications, including touching, compression, and stretching. For highly compressive 3D sensors, bending-dominated structures, such as simple cubic and Kelvin cell structures, are expected to be more susceptible to compressive stress. Among the bending structures, the Kelvin cell structure exhibits a higher relative density than the simple cubic structure, suggesting that it contains a larger number of magnetic microparticles in the same volume. Hence, we selected a Kelvin cell structure for the design of our HCMSs as it incorporates larger magnetic microparticles due to its bending-dominated structure, producing larger magnetic flux changes under identical compression (Figure 2c and Table S1). By conducting a cyclic compression test with four recovery periods, we verified that the Kelvin cell structure can be easily compressed and recovered to its initial state (Figure 2d). Additionally, we conducted simulations using commercial finite-element analysis software ABAQUS under identical conditions, considering the magnetic and mechanical properties of the Kelvin cell structure. The simulation results (ii) show good agreement with the experimental results (i), as shown in Figure 2e.

2.3. Magnetic Characterization of HCMS Materials.

To demonstrate that we can program not only the mechanical properties but also the material properties of the HCMS, which critically affect the output signal, we investigated Kelvin cell structures with various concentrations of magnetic microparticles and verified their magnetic characteristics. Figure 3a illustrates a magnetic composite consisting of magnetic microparticles embedded in an elastomer matrix. By controlling the mixing ratio of the magnetic microparticles embedded in the elastomer, we can easily adjust the magnetic microparticle concentration of the composite from 30 to 70 wt %, as shown in the scanning electron microscopy (SEM) images (Figure 3b). To investigate the magnetic characteristics of the magnetic composite depending on the magnetic concentration, we measured the magnetic hysteresis loop at different magnetic concentrations with identical magnetization directions. As shown in Figures 3c and S4, a higher concentration of magnetic microparticles leads to a larger magnetization of the magnetic composite, implying that more magnetic domains are aligned in the same direction. As the magnetic microparticle concentration increased from 30, 50 to 70 wt %, the saturation magnetization also increased from 34.63, 63.64, and 90.254 emu/g, respectively (Figure 3d). To verify that magnetic composites with various concentrations can be uniformly injected into the internal channel of the 3D-printed sacrificial mold to fabricate HCMSs, we visualized the magnetic microparticle distribution within the $2 \times 2 \times 2$ K cell structures using a nondestructive and in situ imaging system. Figure 3e shows micro-CT images of Kelvin cell structures with 30, 50, and 70 wt % magnetic microparticles distributed in the whole structure. The magnetic microparticles interfere with the X-ray transmittance through the Kelvin cell structures. Hence, the brightness of the micro-CT images represents the distribution of magnetic microparticles, with darker micro-CT images implying a larger number of magnetic microparticles. Because structures with higher magnetic microparticle concentrations produce higher magnetic flux densities, we selected a Kelvin cell structure with 70 wt % magnetic microparticle concentration as a unit cell/composition for our HCMSs. Then, we investigated its magnetic flux density change in the initial and compressed states, giving the HCMSs' output signal (Figures 3f and S5). Figure 3g shows the magnetic density mapping of the bottom surface of several $2 \times 2 \times 2$ K cell structures in the initial state and compressed states. When the $2 \times 2 \times 2$ K cell structure with 70 wt % is compressed by up to 75% strain, the overall structure is deformed, resulting in a variation of both the magnetization profiles and the magnetic microparticle densities. The changes in magnetic flux are predominantly influenced by the variations in the magnetic microparticle concentration within the unit volume of the compressed magnetic section. This phenomenon is more dominant than the effects caused by randomization of the magnetization profile within the magnetic material due to compressive strain. Thus, when the magnetic component is compressed, the magnetic flux passing through the electrical component increases because the concentration of magnetic microparticles in the structure becomes more concentrated. To compare the total magnetic flux density passing through the bottom surface in each state, we calculated the integral of the magnetic flux density measured at evenly distributed points throughout the structure. Figure 3h shows that the total magnetic flux density increases from 5697 to 7618 mT. The increase in magnetic flux density generates an output voltage when the magnetic component is attached to the electrical component, following Faraday's law.
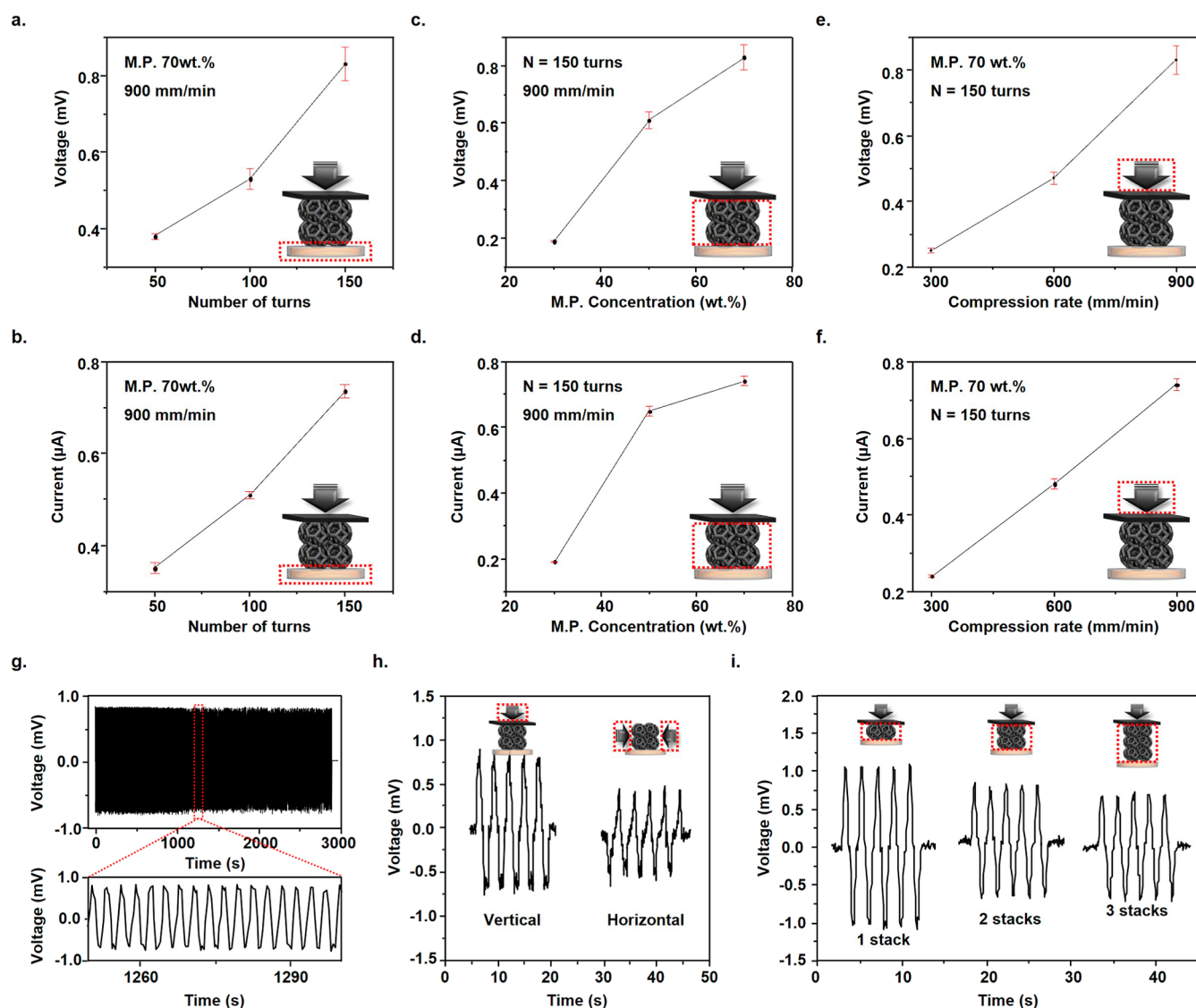
Figure 4. Sensing performance of the HCMSs. (a,b) Output voltage and current of the HCMSs with various numbers of coil turns; 50, 100, and 150 turns. (c,d) Output voltage and current of the HCMSs with various magnetic particle concentrations; 30, 50, and 70 wt %. (e,f) Output voltage and current of the HCMSs with various compression rates; 300, 600, and 900 mm/min. (g) Output voltages of the HCMSs after 1000 cycles during the mechanical durability test. (h) Output voltages of HCMSs with different mechanical stimuli directions which demonstrate anisotropic mechanoelectrical conversion. (i) Output voltages of HCMSs with various stacking layers; 1, 2, and 3 layers. Three HCMSs with 1, 2, and 3 layers stacked by 7 mm, using the same compression rate and duration. (a−i) Details regarding the constants and variables for all measurements can be found in Table S2 in the Supporting Information file.

2.4. Sensing Characterization of the HCMS. We analyzed the output performance of HCMSs with various parameters that are closely related to the number of turns (N), the total magnetic flux change ($\Delta\varphi$), and the compression time of HCMSs (Δt), as given in eq 1. The HCMSs containing a z-axis magnetized $2 \times 2 \times 2$ K cell structure were compressed to 75% strain to investigate the relationship between parameters such as N, $\Delta\varphi$, and Δt, and the output performance, as shown in Figure 4a−h. According to eq 1, the number of turns in the coils and the magnetic flux change are directly proportional to the output voltage, whereas the compression time of the HCMSs is inversely proportional to the output voltage. These theoretical predictions are in good agreement with the experimental results in Figure 4a−f. Hence, we developed HCMSs with various numbers of turns in the electrical component and embedded 70 wt % magnetic microparticles in the elastomer matrix. As the number of turns increased from

50 to 150, the output voltage and current also increased from 0.38 to 0.83 mV and 0.35 to 0.74 μA, respectively (Figure 4a,b). Moreover, we investigated the impact of different magnetic microparticle concentrations on the output performance of the HCMSs while maintaining the number of turns of the coil at 150. Figure 4c,d shows that increasing the magnetic microparticle concentration from 30 to 70 wt % enhances the output voltage and current from 0.18 to 0.83 mV and 0.19 to 0.74 μA, respectively. Figure 4a−d shows the results of a compression test at 900 mm/min up to 75% strain. Moreover, to demonstrate how the compression time of the HCMSs affects the output performance of the HCMSs, we performed compression tests at different compression rates, as shown in Figure 4e,f. Decreasing the compression rate from 900 to 300 mm/min increases the compression time of the HCMSs for 75% strain, causing the output voltage and current to drop from 0.83 to 0.25 mV and from 0.74 to 0.24 μA, respectively.
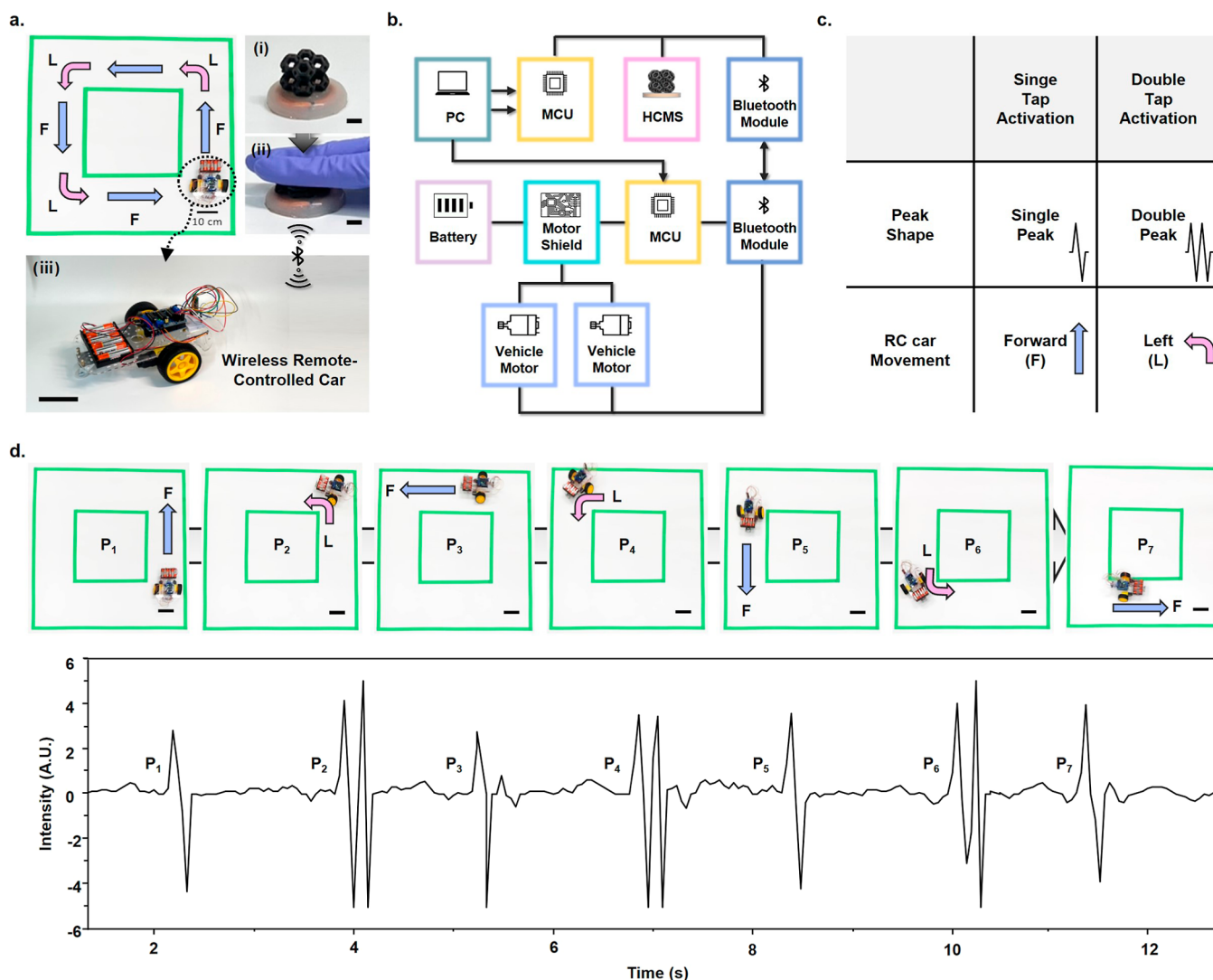
Figure 5. Demonstration of the robotic operation using a HCMS. (a) Overview of the RC car demonstration for track navigation. (i) Initial state of the HCMS with a scale bar of 10 mm. (ii) Compressed state of the HCMS with a scale bar of 10 mm. (iii) RC car wirelessly connected to the HCMS with a scale bar of 100 mm. (b) Hardware architecture of the system. (c) Feature table for robotic control varying by activation modes. (d) Manual control process for track navigation accompanied by the corresponding sensor. Scale bar is 100 mm.

After confirming that a larger number of coils, higher magnetic microparticle concentrations, and a higher compression rate facilitate a higher output performance, we fabricated HCMSs containing a coil with 150 turns and 70 wt % magnetic microparticle concentrations and applied a compression rate of 900 mm/min, as shown in Figure 4g−i. Furthermore, the durability of HCMS was evaluated by a cyclic compression test with a compression/recovery process of 1000 cycles. As shown in Figure 4g, even after 1000 compression/recovery cycles, the output voltage was sustained, suggesting a long working life and excellent reliability. After the durability test, we further investigated the output voltage along the mechanical stimuli direction. As previously reported, 3D magnetoelastic sensors exhibit anisotropic mechanoelectrical conversion behavior depending on the mechanical stimuli direction.[24,25] The output voltage always exhibits alternating current (AC) electrical signals, regardless of the mechanical stimuli direction. However, the phase-shifted signals are measured depending on the direction of the mechanical stimuli. As shown in Figures 4h and S6, the anisotropic mechanoelectrical conversion behavior was confirmed. Compression tests with vertical and horizontal

loading directions were conducted at a compression rate of 900 mm/min with up to 75% strain. The output voltages obtained from these tests varied, suggesting that the correlation between the initial magnetic flux value and the compressed state varies depending on the direction of the mechanical stimulus. Vertical and horizontal compression tests yielded HCMS output voltages of 0.81 and 0.40 mV, respectively. In addition to controlling various parameters that affect the output performance of HCMSs with $2 \times 2 \times 2$ K cell structures, we investigated the output performance in dependence on the design parameter, as shown in Figures 4i and S7. To this end, we designed HCMSs with different stacking numbers of magnetic Kelvin cell structures and coils with identical numbers of turns and diameters. Then, we uniformly compressed three HCMSs comprising 1, 2, and 3 stacked layers by 7 mm using the same compression rate and duration. Although the compression time, number of turns, and compression heights are identical, the magnetic flux change values obtained with eq 1 vary. As the stacking number of the magnetic Kelvin cell structures increased from 1 to 3, the magnetic flux change passing through the coil decreased with
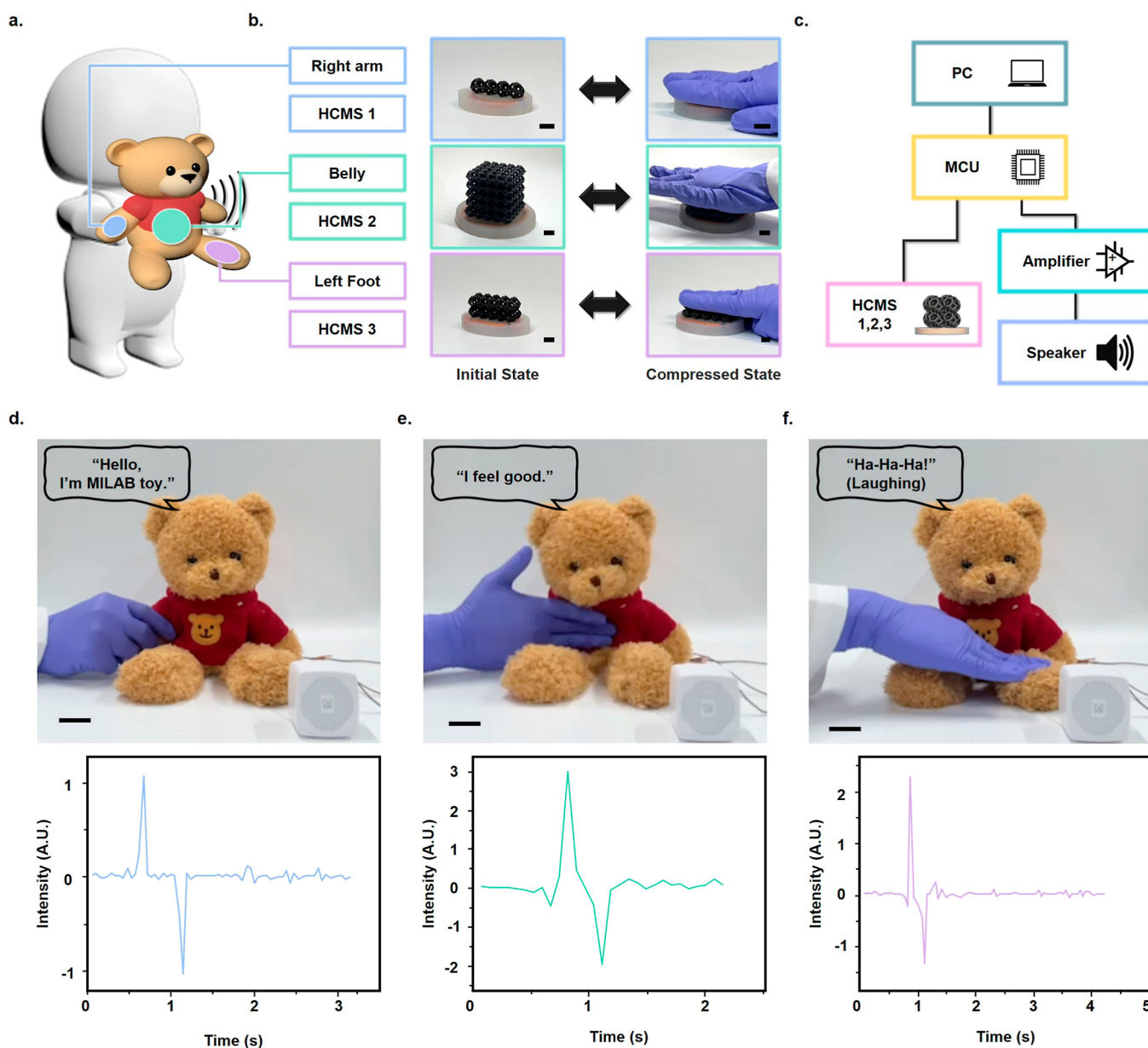
Figure 6. Demonstration of robotic perception using HCMSs. (a) Overview of the toy that produces different dialogues when various body parts are compressed. (b) HCMSs of varying sizes in both their initial and compressed states, embedded in different parts of the toy; a $4 \times 1 \times 1$ HCMS in the right arm, a $5 \times 5 \times 5$ HCMS in the belly, and a $5 \times 2 \times 2$ HCMS in the left foot. Scale bars are 10 mm. (c) Robotic hardware framework. (d) Demonstration of the toy issuing a greeting when its right arm is compressed, with the corresponding output signal. Scale bar is 25 mm. (e) Demonstration of the toy expressing its feelings when its belly is gently pushed, with the corresponding output signal. Scale bar is 25 mm. (f) Demonstration of the toy producing laughter when its left foot is compressed, with the corresponding output signal. Scale bar is 25 mm.

an increasing gap distance. As a result, the HCMS output voltage decreased from 1.03 to 0.67 mV, indicating that the programmable design parameters allow us to control the output performance, even if the HCMSs contain identical cross-sectional areas.

2.5. Application of HCMSs. To demonstrate the potential of HCMSs in real-world applications, we constructed two different robotic systems with different form factors. Due to its programmable physical properties, HCMS offers advantages in detecting and encoding diverse haptic interactions for specific tasks, potentially enhancing user experiences when interacting with daily 3D objects. As shown in Figure 5 and Movie S1, the first system presents an HCMS structured in a Kelvin cell design that serves as a control unit for remote operation.

Figure 5a provides a comprehensive view of the HCMS's practical implementation, specifically in the context of controlling a robot such as an RC car.[32] We constructed a track and devised a navigation plan for an RC car. Depending on the compression state of the HCMS, the RC car, which is wirelessly connected to the HCMS, receives commands to determine its movements. Owing to its high compressibility, $2 \times 2 \times 2$-sized HCMSs exhibit high durability and a wide dynamic range. These characteristics, enabling the sensor to withstand and detect a wide range of forces, render it an excellent candidate for a control unit. In addition, we developed a flow process system for the circuit, as shown in Figure 5b. Specifically, when the HCMS is compressed, output signals are generated. These signals are then picked up by a

master Bluetooth module connected to a microcontroller and transmitted to a slave Bluetooth module from which a second microcontroller reads the data. Based on these data, the microcontroller decides whether the RC car will move forward or make a left turn. To achieve a successful demonstration, we established a preset threshold value for the sensor signals after minimizing the noise through filtering. The output signal exhibits distinct behavior: it increases when the HCMS is compressed and decreases upon release. Therefore, we designated separate threshold values for both the onset and the cessation of sensor deformation. Taking this behavior into account, we established a protocol where a single tap activation (resulting in one signal peak) instructs the RC car to move forward, while a double tap activation (yielding a double peak) directs it to turn left. This strategy, depicted in Figure 5c, allows for a clear differentiation of commands. The manual control process for the RC car's track navigation, along with the corresponding sensor signals, is shown in Figure 5d. To go around the first curve, the RC car is guided by a sequence of signal peaks: a single peak ($P_{1,3,5,7}$) instructs it to go forward, while a double peak ($P_{2,4,6}$) instructs it to turn left. This pattern is repeated until the RC car returned to its starting position. Apart from robot operation, Figure 6 demonstrates that HCMSs can also serve as robotic perception units. This is illustrated by our creation of a talking teddy bear, as depicted in Movie S2. As shown in Figure 6a,b, to interact with users, three soft HCMSs of varying volumes and shapes are integrated into distinct parts of the stuffed toy's body: right arm, belly, and left foot. Due to their programmable flexibility, high compressibility, and designable 3D shape, the sensors maintain the toy's original shape and preserve natural touch sensation, even when the toy's internal cotton is removed. Thus, HCMS perception units allow seamless integration of robotic units with the object body as well as independent design of the 3D volumetric shape and mechanical flexibility of the sensor. Depending on which body part the user interacts with, the toy produces different dialogues, thereby facilitating human interactions. Figure 6c provides an overview of the process flow for the robotic perception system. Three HCMSs are linked to the microcontroller's three analog pins, while the speaker connected to the amplifier utilizes digital pins. All sensors share identical parameters, such as magnetic micro-particle size, microparticle concentration, number of coil turns, and coil thickness. However, due to the sensing mechanism of the HCMS, sensors with larger coil diameters and higher stacking layers—which contribute to a larger overall sensor volume—exhibit a more substantial flux change. Consequently, the magnitude of the output signal is influenced. This necessitates the establishment of a distinct range of threshold values corresponding to each sensor volume. When pressed, akin to a handshake, the $4 \times 1 \times 1$ sized HCMS embedded within the right arm triggers the toy to utter a greeting: "Hello, I'm a MILAB toy", as shown in Figure 6d. When a user gently taps the toy's belly, where a $5 \times 5 \times 5$ sized HCMS is embedded, the toy voices the phrase "I feel good", as shown in Figure 6e. When the toy's left foot, housing a $5 \times 2 \times 2$ sized HCMS, is tapped, akin to a human tickling its foot, it responds with a laughter sound, as shown in Figure 6f.

3. CONCLUSIONS

In summary, we have developed HCMSs with programmable 3D shapes, scales, and mechanical properties. These sensors are less affected by environmental factors, thus exhibiting numerous advantages for HMI applications. The HCMSs were fabricated by employing a 3D-printed sacrificial mold, which allowed us to fabricate predesigned 3D structures by injecting magnetic composites into the internal channel of a sacrificial mold. This fabrication process expands the design possibilities for HCMS, including material selection, lattice unit structure, sensor size, shape, and more. We tuned the sensing performance of HCMSs based on Faraday's law by adjusting the form factor, magnetic microparticle concentration, layer number of coiled wires, and other parameters related to the compressing conditions. Two different robotic systems using HCMSs demonstrate the potential of overcoming the limitations of magnetoelastic sensors observed in previous studies, exhibiting high compressibility, wide dynamic range, and efficient structural integration in 3D objects. Thus, we envision that HCMS can be further used to obtain diverse user interaction patterns in daily life objects, facilitating elaborate human−object interactions and widening the application area of HMI devices in daily life.

4. EXPERIMENTAL SECTION

Fabrication of HCMSs: first, a PVA sacrificial mold with an internal channel network was fabricated using a commercial 3D-Printer (Ultimaker 3). Second, a liquid state elastomer composed of Ecoflex 00-30 (Smooth-on) and PDMS (Sylgard 184, Dow Corning) was mixed with neodymium−iron−boron (NdFeB, MQFP-15-7-20065-089, Magnequench) microparticles with an average size of 5 μm to create a magnetic composite. Here, two prepolymers of Ecoflex 0030 were combined with two prepolymers of PDMS with weight ratios of 1:1 and 9:1, respectively. The magnetic composite contained neodymium−iron−boron magnetic microparticles in weight percen-tages, ranging from 30 to 70 wt %. Third, a syringe was used to inject the liquid magnetic composite into the internal channel network. When the composite could not further penetrate the channel, the mold was wrapped with aluminum foil to keep the composite from leaking out of the channel. Fourth, the wrapped mold was placed on a hot plate at 80 °C for 6 h to polymerize the magnetic composite. Then, the foil was peeled off, and the mold was put into a water bath to dissolve the water-soluble PVA mold. The dissolving process afforded a polymerized magnetic composite, which we named magnetic lattice structure. The magnetic lattice structure was magnetized at 1500 V with a magnetizer (MCB-3530M, SCMI). The magnetization was aligned with the z-axis, parallel to the vertical pressure direction. Finally, the magnetic lattice structure was attached to a copper coil with a 0.2 mm thickness and embedded in an elastomer. The number of turns of the coil was 50, 100, and 150.

Mechanical characterization of the magnetic lattice structures of HCMSs: the mechanical properties of the magnetic lattice structures were investigated by using a universal testing machine (UTM, AGX-100NX, and SHIMADZU). To obtain stress−strain curves of various 3D-printed structures, 3D solid cubic, simple cubic, Kelvin cell, and octet truss structures sized $20 \times 20 \times 20$ mm^3 were subjected to compression tests at 10 mm/min.

Magnetic characterization of the magnetic lattice structures of HCMSs: the magnetic hysteresis loops of magnetic composites with different concentrations were obtained under an external magnetic field ranging from −2.7 to 2.7 T using a vibrating sample magnetometer (VSM, EZ9, MicroSense). The magnetic flux density was measured by using a Gauss meter (GM-197, Metravi). To ensure the accurate and precise movement of the Gauss meter, we utilized a 3D printer (M3-ID, MAKERGEAR).

Electrical performance characterization of HCMSs: magnetoelastic output signals were measured in vertical and horizontal contact separation modes. The HCMSs were periodically compressed with a UTM (AGX-100NX, SHIMADZU Inc.) under different conditions. The electrical performance of HCMS was measured by a data

acquisition and multimeter system (DMM 7510, Tektronix) with an internal impedance of 1 MΩ.

Imaging and videography: images and videos of the HCMSs and magnetic lattice structures were taken using a commercial smartphone camera (Apple iPhone 12). The magnetic particle distribution was scanned with SEM (Nova NanoSEM) and X-ray microcomputed tomography (micro-CT, Skyscan1176, Bruker).

Finite-Element Analysis: finite-element analysis was performed using commercially available ABAQUS software[33] to predict the deformation of the magnetic lattice structure under compression tests. The magnetic lattice structure was designed using the 3D modeling software nTopology and imported into ABAQUS. All elements were defined as a four-node linear tetrahedron (C3D4). The material properties and the strain energy function were set as hyperelastic using a polynomial function with $N = 2$. The material coefficient parameters were verified by fitting the experimentally measured stress−strain curves and obtained as D1 = D2 = 0, C10 = −0.0693 MPa, C01 = 0.2678 MPa, C20 = 0.0229 MPa, C11 = −0.3168 MPa, and C02 = 0.7737 MPa. Then, bottom and top rigid plates were added to the magnetic lattice structure to apply boundary conditions. While the encastre boundary condition[33] was applied to the bottom plate, the top rigid plate was subjected to external stress in a downward direction.

■ ASSOCIATED CONTENT

ⓈⒾ Supporting Information

The Supporting Information is available free of charge at https://pubs.acs.org/doi/10.1021/acsami.3c13638.

> Maxwell number and relative density of various lattice structures; experimental results for a compression test for magnetic structures; magnetic flux density measurement using a 3D printer; anisotropic mechanoelectrical conversion behavior of HCMS with $2 \times 2 \times 2$ K cell structure; output current of the HCMSs with different stacking number of magnetic Kelvin cell structure; and charging curves of 0.1 and 1.0 μF capacitors by hand tapping the HCMS with $5 \times 5 \times 5$ K cell structure (PDF)
>
> Robot operation application (MP4)
>
> Robot perception application (MP4)

■ AUTHOR INFORMATION

Corresponding Author

Jiyun Kim − *School of Materials Science and Engineering, Ulsan National Institute of Science and Technology, Ulsan 44919, South Korea; Center for Multidimensional Programmable Matter, Ulsan National Institute of Science and Technology, Ulsan 44919, South Korea;* Email: jiyunkim@unist.ac.kr

Authors

Hyeonseo Song − *School of Materials Science and Engineering, Ulsan National Institute of Science and Technology, Ulsan 44919, South Korea;* ⓞ orcid.org/0000-0003-3722-414X

Yeonwoo Jang − *School of Materials Science and Engineering, Ulsan National Institute of Science and Technology, Ulsan 44919, South Korea;* ⓞ orcid.org/0000-0002-8636-4432

Jin Pyo Lee − *School of Materials Science and Engineering, Nanyang Technological University, Singapore 639798, Singapore*

Jun Kyu Choe − *School of Materials Science and Engineering, Ulsan National Institute of Science and Technology, Ulsan 44919, South Korea*

Minbyeol Yun − *Powder Materials Division, Korea Institute of Material Science, Changwon 51508, South Korea*

Youn-Kyoung Baek − *Powder Materials Division, Korea Institute of Material Science, Changwon 51508, South Korea*

Complete contact information is available at:
https://pubs.acs.org/10.1021/acsami.3c13638

Author Contributions

#H.S. and Y.J. are contributed equally to this work. H.S., Y.J., and J.K. conceived the project, designed the studies, and analyzed the results. H.S., Y.J., J.L., and J.C. conducted the experiments. H.S., Y.J., Y.B., and J.K. wrote and revised the manuscript.

Notes

The authors declare no competing financial interest.

■ ACKNOWLEDGMENTS

■ ABBREVIATIONS

3D, three-dimensional; HMI, human−machine interface; 2D, two-dimensional; TPU, thermoplastic polyurethane; RC, remote-controlled; PVA, poly(vinyl alcohol); NdFeB, neodymium−iron−boron; HCMS, highly compressible magnetoelastic sensor; SC_1, solid cubic; SC_2, simple cubic; KC, Kelvin cell; OT, octet truss; AC, alternating current; UTM, universal testing machine; VSM, vibrating sample magnetometer; DMM, digital multimeter; micro-CT, microcomputed tomography

■ REFERENCES

(1) Biswas, S.; Visell, Y. Haptic Perception, Mechanics, and Material Technologies for Virtual Reality. *Adv. Funct. Mater.* **2021**, *31* (39), 2008186.

(2) Ghosh, S. K.; Mandal, D. Synergistically Enhanced Piezoelectric Output in Highly Aligned 1D Polymer Nanofibers Integrated All-Fiber Nanogenerator for Wearable Nano-Tactile Sensor. *Nano Energy* **2018**, *53*, 245−257.

(3) Hiramatsu, T.; Kamei, M.; Inoue, D.; Kawamura, A.; An, Q.; Kurazume, R. Development of Dementia Care Training System Based on Augmented Reality and Whole Body Wearable Tactile Sensor. *2020 IEEE/RSJ International Conference on Intelligent Robots and Systems (IROS)*; Institute of Electrical and Electronics Engineers, 2020; pp 4148−4154.

(4) Liao, X.; Song, W.; Zhang, X.; Zhan, H.; Liu, Y.; Wang, Y.; Zheng, Y. Hetero-Contact Microstructure to Program Discerning Tactile Interactions for Virtual Reality. *Nano Energy* **2019**, *60*, 127−136.

(5) Lin, W.; Wang, B.; Peng, G.; Shan, Y.; Hu, H.; Yang, Z. Skin-Inspired Piezoelectric Tactile Sensor Array with Crosstalk-free Row+ Column Electrodes for Spatiotemporally Distinguishing Diverse Stimuli. *Adv. Sci.* **2021**, *8* (3), 2002817.

(6) Pyo, S.; Lee, J.; Bae, K.; Sim, S.; Kim, J. Recent Progress in Flexible Tactile Sensors for Human-Interactive Systems: from Sensors to Advanced Applications. *Adv. Mater.* **2021**, *33* (47), 2005902.

(7) Zhong, W.; Ming, X.; Li, W.; Jia, K.; Jiang, H.; Ke, Y.; Li, M.; Wang, D. Wearable Human-Machine Interaction Device Integrated by All-Textile-Based Tactile Sensors Array via Facile Cross-Stitch. *Sens. Actuators, A* **2022**, *333*, 113240.

(8) Liu, Y.; Yiu, C.; Song, Z.; Huang, Y.; Yao, K.; Wong, T.; Zhou, J.; Zhao, L.; Huang, X.; Nejad, S. K.; et al. Electronic Skin as Wireless Human-Machine Interfaces for Robotic VR. *Sci. Adv.* **2022**, *8* (2), No. eabl6700.

(9) Zhang, S.; Xiao, Y.; Chen, H.; Zhang, Y.; Liu, H.; Qu, C.; Shao, H.; Xu, Y. Flexible Triboelectric Tactile Sensor Based on a Robust MXene/Leather Film for Human-Machine Interaction. *ACS Appl. Mater. Interfaces* **2023**, *15* (10), 13802−13812.

(10) Yao, G.; Xu, L.; Cheng, X.; Li, Y.; Huang, X.; Guo, W.; Liu, S.; Wang, Z. L.; Wu, H. Bioinspired Triboelectric Nanogenerators as Self-Powered Electronic Skin for Robotic Tactile Sensing. *Adv. Funct. Mater.* **2020**, *30* (6), 1907312.

(11) Kaur, M.; Kim, T. H.; Kim, W. S. New Frontiers in 3D Structural Sensing Robots. *Adv. Mater.* **2021**, *33* (19), 2002534.

(12) Fan, F.-R.; Tian, Z.-Q.; Lin Wang, Z. Flexible Triboelectric Generator. *Nano energy* **2012**, *1* (2), 328−334.

(13) Wang, X.; Zhang, Y.; Zhang, X.; Huo, Z.; Li, X.; Que, M.; Peng, Z.; Wang, H.; Pan, C. A Highly Stretchable Transparent Self-powered Triboelectric Tactile Sensor With Metallized Nanofibers for Wearable Electronics. *Adv. Mater.* **2018**, *30* (12), 1706738.

(14) Wang, J.; Cui, P.; Zhang, J.; Ge, Y.; Liu, X.; Xuan, N.; Gu, G.; Cheng, G.; Du, Z. A Stretchable Self-Powered Triboelectric Tactile Sensor with EGaIn Alloy Electrode for Ultra-Low-Pressure Detection. *Nano Energy* **2021**, *89*, 106320.

(15) Lu, D.; Liu, T.; Meng, X.; Luo, B.; Yuan, J.; Liu, Y.; Zhang, S.; Cai, C.; Gao, C.; Wang, J.; et al. Wearable Triboelectric Visual Sensors for Tactile Perception. *Adv. Mater.* **2023**, *35* (7), 2209117.

(16) Lai, Q. T.; Zhao, X. H.; Sun, Q. J.; Tang, Z.; Tang, X. G.; Roy, V. A. Emerging MXene-Based Flexible Tactile Sensors for Health Monitoring and Haptic Perception. *Small* **2023**, *19*, 2300283.

(17) Hu, Y.; Wang, Z. L. Recent Progress in Piezoelectric Nanogenerators as a Sustainable Power Source in Self-Powered Systems and Active Sensors. *Nano Energy* **2015**, *14*, 3−14.

(18) Cao, X.; Xiong, Y.; Sun, J.; Zhu, X.; Sun, Q.; Wang, Z. L. Piezoelectric Nanogenerators Derived Self-Powered Sensors for Multifunctional Applications and Artificial Intelligence. *Adv. Funct. Mater.* **2021**, *31* (33), 2102983.

(19) Lee, E. I.; Park, J. W. A Self-Powered, Single-Mode Tactile Sensor Based on Sensory Adaptation Using Piezoelectric-Driven Ion Migration. *Adv. Mater. Technol.* **2022**, *7* (12), 2200691.

(20) Fu, R.; Tu, L.; Guan, Y.; Wang, Z.; Deng, C.; Yu, P.; Tan, G.; Ning, C.; Zhou, L. Intrinsically Piezoelectric Elastomer Based on Crosslinked Polyacrylonitrile for Soft Electronics. *Nano Energy* **2022**, *103*, 107784.

(21) Zhou, Y.; Zhao, X.; Xu, J.; Fang, Y.; Chen, G.; Song, Y.; Li, S.; Chen, J. Giant Magnetoelastic Effect in Soft Systems for Bioelectronics. *Nat. Mater.* **2021**, *20* (12), 1670−1676.

(22) Chen, G.; Zhao, X.; Andalib, S.; Xu, J.; Zhou, Y.; Tat, T.; Lin, K.; Chen, J. Discovering Giant Magnetoelasticity in Soft Matter for Electronic Textiles. *Matter* **2021**, *4* (11), 3725−3740.

(23) Zhao, X.; Zhou, Y.; Xu, J.; Chen, G.; Fang, Y.; Tat, T.; Xiao, X.; Song, Y.; Li, S.; Chen, J. Soft Fibers with Magnetoelasticity for Wearable Electronics. *Nat. Commun.* **2021**, *12* (1), 6755.

(24) Zhang, X.; Ai, J.; Ma, Z.; Du, Z.; Chen, D.; Zou, R.; Su, B. Magnetoelectric Soft Composites with a Self-Powered Tactile Sensing Capacity. *Nano Energy* **2020**, *69*, 104391.

(25) Wu, H.; Zhang, X.; Ma, Z.; Zhang, C.; Ai, J.; Chen, P.; Yan, C.; Su, B.; Shi, Y. A Material Combination Concept to Realize 4D Printed Products with Newly Emerging Property/Functionality. *Adv. Sci.* **2020**, *7* (9), 1903208.

(26) Wu, H.; Wang, Q.; Wu, Z.; Wang, M.; Yang, L.; Liu, Z.; Wu, S.; Su, B.; Yan, C.; Shi, Y. Multi-Material Additively Manufactured Magnetoelectric Architectures with a Structure-Dependent Mechanical-to-Electrical Conversion Capability. *Small Methods* **2022**, *6* (12), 2201127.

(27) Faraday, M. LIV. Experimental Researches in Electricity—Fifteenth Series. *Lond. Edinb. Dublin Philos. Mag. J. Sci.* **1839**, *15* (97), 358−372.

(28) Lu, B.; Lan, H.; Liu, H. Additive manufacturing frontier: 3D Printing Electronics. *Opto-Electron. Adv.* **2018**, *1* (1), 170004.

(29) Yeo, S. J.; Oh, M. J.; Yoo, P. J. Structurally Controlled Cellular Architectures for High-Performance Ultra-Lightweight Materials. *Adv. Mater.* **2019**, *31* (34), 1803670.

(30) Wang, Y.; Li, L.; Hofmann, D.; Andrade, J. E.; Daraio, C. Structured Fabrics with Tunable Mechanical Properties. *Nature* **2021**, *596* (7871), 238−243.

(31) Mao, A.; Zhao, N.; Liang, Y.; Bai, H. Mechanically Efficient Cellular Materials Inspired by Cuttlebone. *Adv. Mater.* **2021**, *33* (15), 2007348.

(32) Xu, J.; Tat, T.; Zhao, X.; Zhou, Y.; Ngo, D.; Xiao, X.; Chen, J. A Programmable Magnetoelastic Sensor Array for Self-Powered Human-Machine Interface. *Appl. Phys. Rev.* **2022**, *9* (3), 031404.

(33) Smith, M. *ABAQUS/Standard User's Manual*, version 6.9, 2009 .